ChemComm

COMMUNICATION

View Article Online
View Journal | View Issue

Cite this: *Chem. Commun.*, 2024, **60**, 10001

Received 12th June 2024,
Accepted 12th August 2024

DOI: 10.1039/d4cc02844a

rsc.li/chemcomm

A high-power 4 × 4: crystallographic and electrochemical insights into a novel Wadsley–Roth anode $Nb_9Ti_{1.5}W_{1.5}O_{30}$†

Elizabeth Helen Driscoll, *[abc] Alex Green, [bc] Dominic Fortes, [d] Christopher Howard, [d] Laura Louise Driscoll, [bc] Emma Kendrick, [ac] Colin Greaves [b] and Peter Raymond Slater *[bc]

A novel 4 × 4 Wadsley–Roth block phase, $Nb_9Ti_{1.5}W_{1.5}O_{30}$, has been prepared and its structure determined through Neutron and X-ray diffraction studies. Electrochemical testing indicated excellent high rate performance, with a returned delithiation capacity of 184 (4) mA h g^{-1} at a current of 2 A g^{-1}.

With the transition towards Net Zero and mitigating the growing and apparent effects of climate change, the use of efficient energy storage is at the forefront of meeting this challenge. While conventional Li ion batteries utilising a graphite anode are appropriate for many applications, there is a need for higher power (fast charge/discharge) batteries for applications such as for consumer devices (power tools) and heavy duty transport modes (trains and earth movers). In this respect, ($Li_4Ti_5O_{12}$, LTO) has found applications as a commercial anode, and comprises 4% of the global market share for anodes.[1] Nevertheless this leads to a lower energy density cell, which derives from the high operating voltage (*ca.* 1.5 V, rather than 0 V for graphite *vs.* Li/Li^+),[2] as well as reduced theoretical capacities (175 *vs.* 372 mA h g^{-1} for LTO and graphite respectively). Consequently, alternative high-power anode chemistries,[3] which combine the safety and lifetime benefits of LTO, while providing higher energy density are sought. In this respect, niobium oxide based systems are attracting considerable interest. These materials have the ability to operate at fast charge/discharge (≤6 minutes) and have higher energy density than LTO cells, due to the potential of the dual redox couples of niobium: Nb^{5+}/Nb^{4+} and Nb^{4+}/Nb^{3+}, rather than singular Ti^{4+}/Ti^{3+} as allowed in LTO.

(Metal-doped) Niobium oxides for this application are classically a Wadsley–Roth (WR) block structure, which have oxygen-deficient structures derived from ReO_3 crystal structure, and commonly formed for compositions of NbO_2–Nb_2O_5,[4] TiO_2–Nb_2O_5,[4] WO_3–Nb_2O_5.[5] To compensate for the oxygen off-stoichiometry within these systems, crystallographic shear planes exist, in addition to tetrahedral cations[6] in some cases, to form varying degrees of block sizes (defined by $n \times m$ – width × length). The WR structures are stable hosts for lithium intercalation, as detailed by Griffith *et al.*[7] The simplest undoped niobium oxide WR structure is H-Nb_2O_5 (the high temperature polymorph) with a $(3 \times 5)_\infty$ and $(3 \times 4)_1$ block structure. This has good electrochemical performance at low rates, although the high pressure[8]-low-temperature polymoprh T-phase, (alternative Tungsten Bronze structure) is reported to maintain its capacity better at high rates (albeit the initial starting capacity is lower).[9]

Considering the titanium doped niobates, a variety of block sizes are possible. $TiNb_2O_7$ (TNO),[10] a well established material, has the smallest block size (3 × 3). Decreasing the Ti content, results in the formation of a larger block size, as seen in the materials $Ti_2Nb_{10}O_{29}$[11] and $TiNb_{24}O_{62}$.[12]

Griffith *et al.* have investigated W-doped niobates extensively, in particular $Nb_{16}W_5O_{55}$ and $Nb_{18}W_{16}O_{93}$.[13] In original reports, the former material was found to return a capacity of 148 mA h g^{-1} (*ca.* 3.4 A g^{-1}; 20C),[13] while more recent reports[14] find the material to have an average discharge capacity of 101 mA h g^{-1} at 4 A g^{-1}. Recent work has questioned the existence of the $Nb_{18}W_{16}O_{93}$ phase and instead suggested that this "phase" is related to known $Nb_8W_9O_{47}$ and $Nb_7W_{10}O_{47.5}$ systems (*i.e.* $(Nb,W)_{34}O_{94}$).[15] A schematic showing the block changes with crystal density, for the varying MO_x systems (M = Nb/Ti/W), with resulting theoretical gravimetric capacities is presented in the ESI.† Siffert *et al.* have investigated Nb–Ti–W–O systems, and have reported Ti doped $Nb_{14}W_3O_{44}$ and $Nb_{13.5}W_{20.5}O_{94}$ phases with good performance,[16] highlighting the potential of multication doped systems.

[a] *School of Metallurgy and Materials, University of Birmingham, Edgbaston, B15 2SE, UK. E-mail: e.h.driscoll@bham.ac.uk*
[b] *School of Chemistry, University of Birmingham, Edgbaston, B15 2SE, UK. E-mail: p.r.slater@bham.ac.uk*
[c] *The Faraday Institution, Becquerel Avenue, Harwell, Didcot, OX11 0RA, UK*
[d] *ISIS Neutron and Muon Source, Rutherford Appleton Laboratory, Harwell Campus, Didcot, OX11 0QX, UK*

† Electronic supplementary information (ESI) available. See DOI: https://doi.org/10.1039/d4cc02844a

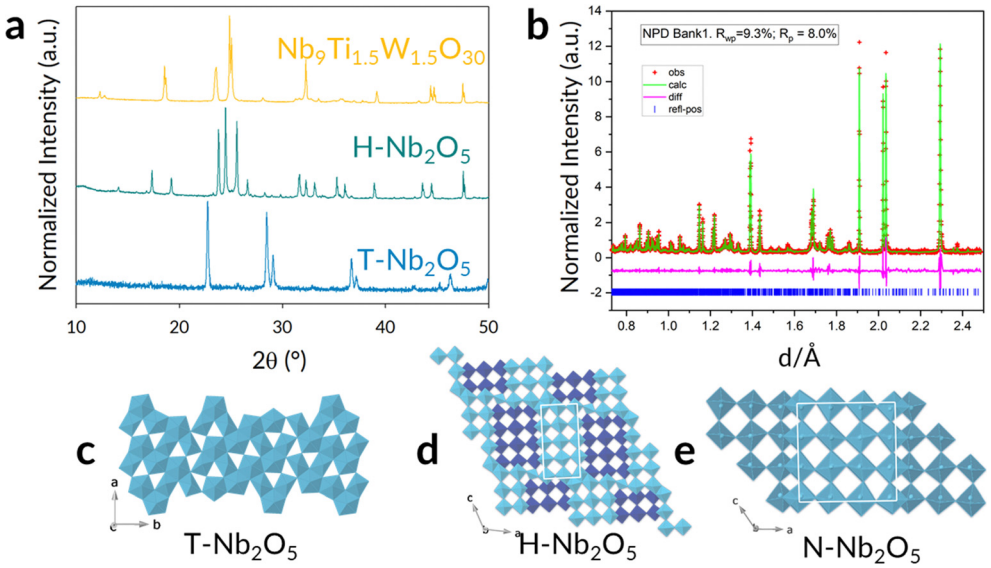

Fig. 1 (a) XRPD pattern of novel $Nb_9Ti_{1.5}W_{1.5}O_{30}$ in comparison to high-(H-phase) and low-temperature (T-phase) Nb_2O_5. (b) Observed, calculated and difference plots of $Nb_9Ti_{1.5}W_{1.5}O_{30}$, determined through Rietveld refinement using the collected Neutron Diffraction data – data bank 1 collected from the high resolution back scatter detector is shown here (bank 2 and 3 are presented in the ESI†). (c)–(e) The crystal structures of three Nb_2O_5 polymorphs: (c) T-Nb_2O_5 a Tungsten bronze structure, (d) H-Nb_2O_5 $(3 \times 5)_\infty$ and $(3 \times 4)_1$ (the subscript represents the blocks' connectivity in the ac plane), and (e) N-Nb_2O_5 (4×4 block).

In this publication, we report the synthesis, structure and electrochemical performance of a new titanium–tungsten doped niobium oxide, $Nb_9Ti_{1.5}W_{1.5}O_{30}$, which was identified by an investigation into the dual Ti + W ≈ 2Nb doping strategy in Nb_2O_5. Noticeably the W content of this phase is lower than recently reported Nb–W–O systems: this reduced W content would reduce the cost, the mass, and use of this critical element (which has greater economic importance risk compared to Nb[17]).

In determining the phase purity and basic crystal structure of the novel material $Nb_9Ti_{1.5}W_{1.5}O_{30}$, the XRPD pattern was collected and is compared with those for the T- and H-Nb_2O_5 phases in Fig. 1a. Notably, the doping strategy resulted in a different XRD pattern, with no evidence for starting reagents; moreover, the pattern strongly resembled that reported for the different Nb_2O_5 polymorph, N-Nb_2O_5,[18–20] a 4×4 block phase that is notoriously difficult to isolate. The differences in structure for the different polymorphs originate from the octahedra bonding, such that the low temperature phase T-Nb_2O_5 is a Tungsten-Bronze structure, whereas the H-Nb_2O_5 and N-Nb_2O_5 polymorphs differ through their block sizes (Fig. 1c–e). Prior to full structural elucidation, a Pawley fit refinement (ESI,† Fig. S3) was performed using the TOPAS suite of programs[21,22] and fitting residuals were found to be: R_{wp} 7.87% and R_p 5.67%. The fit confirms the phase purity and results in unit cell dimensions consistent with a N-Nb_2O_5-type structure.[20]

Gaining further structural information from the XRPD was challenging because of significant preferred orientation effects, and no direct information on the cation distribution or reliable oxygen atom positions was possible. There are eight symmetry-unique cation sites in the N-Nb_2O_5 unit cell and, assuming these to be fully occupied by the Nb, Ti and W atoms, an additional problem presents itself that there may not be a unique cation population that provides the experimental scattering for any given site whether we use XRPD or NPD data. For example, using NPD a site occupied by W has the same scattering as it would have for the occupancy 0.78 Nb and 0.22 Ti. In addition, a site with a random distribution corresponding to an average site occupancy of 0.68 Ti and 0.32 Nb has zero nett scattering and its location would be indeterminable. These issues would normally be overcome by a joint refinement using both XRPD and NPD datasets, and as such, this strategy was adopted for structure analysis and cation distribution. The nuclear neutron scattering factors provide not only precise location of the anions, but also high contrast for the cations. The XRD data were primarily included to eliminate the problems with NPD illustrated above.

Given the potential for slight loss of W *via* volatilization during the synthesis procedure, the sample was analysed using EDS (ESI,† Fig. S4), giving results in agreement with that expected and indicating no W loss. The structure, especially cation ordering, was probed with combined NPD/XRPD histograms and the refinement (using GSAS-II[23]) eventually converged to a realistic and very interesting result; the fit for the NPD high resolution data, bank 1, is shown in Fig. 1b. Full information on the refinement strategy is provided in ESI† together with the other NPD/XRPD data, Fig. S5, ESI.† The resultant structural parameters are detailed in Table S1 (ESI†).

The derived crystal structure displays the distinctive 4×4 block structure of N-Nb_2O_5 but with significant Ti and W cation order. W is fully located on one site, whereas Ti is approximately equally dispersed on two sites, Nb/Ti1 and Nb/Ti2, the occupancies of which are completed by Nb. The unit cell is shown in Fig. 2 and shows two important features:

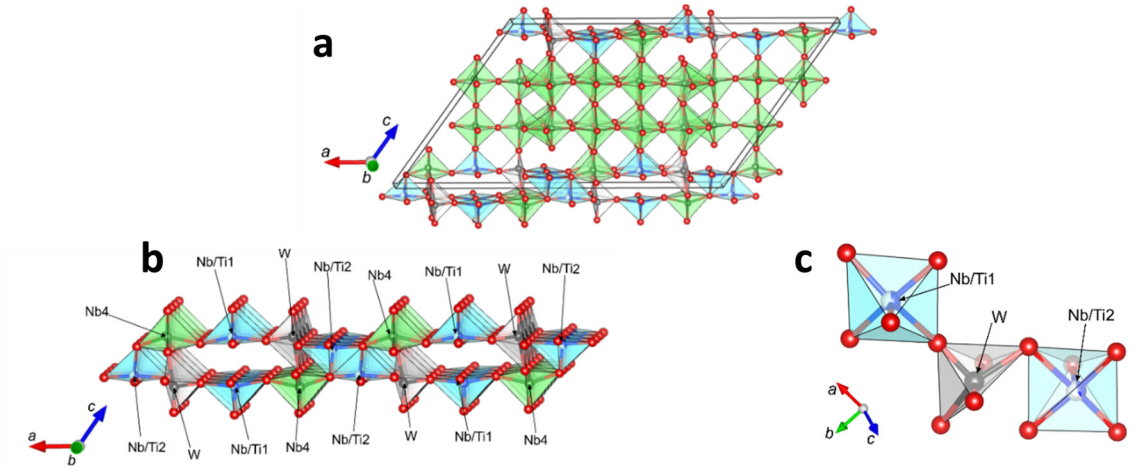

Fig. 2 The structure of $Nb_9Ti_{1.5}W_{1.5}O_{30}$ showing (a) the unit cell with oxygen atoms (red), Nb polyhedra (green), mixed Nb/Ti polyhedra (blue) and W polyhedra (grey); (b) the W and Ti cations localized on chains along [100]; (c) the co-ordination of the sites containing the W and Ti atoms.

(1) the sites containing Ti and W are all located on chains at the edges of the 4 × 4 blocks on (001) planes and directed along [100] (Fig. 2a);

(2) distortions of the Ti- and W-containing polyhedra occur to reduce the coordination number to five and provide empty channels in the structure, running along [010] as visualized in Fig. 2b.

The coordination around both the W and Nb/Ti sites is approximately square pyramidal, as seen in Fig. 2c. The high isotropic displacement parameters (IDPs) for the cations (all constrained equal) reflects the disorder associated with the mixed occupancy of the two Nb/Ti sites and possibly other cation disorder in addition to our simple model. Table S2 (ESI†) shows closest bond distances around the cation sites, which represent an average environment for the mixed occupation Nb/Ti sites. For the square pyramidal W, Nb/Ti1 and Nb/Ti2, the next shortest bond that would complete 6-fold coordination for these sites is at 2.45(1) Å, 2.66(1) Å and 2.65(1) Å, respectively. The bond valence sums (BVS) are indicated and give values for both Ti(IV) and Nb(V) for the Nb/Ti sites.

The location of the substituent W and Ti ions at the edges of the 4 × 4 blocks is not surprising since these regions contain the edge-linked NbO_6 octahedra in the parent phase with their associated distortions which may preferentially provide more favourable sites. In addition, second order Jahn–Teller effects,[24] especially for W, can also stabilise such distortions. Fig. 2c shows that each WO_5 polyhedron is corner-linked to one $(Nb/Ti1)O_5$ and one $(Nb/Ti2)O_5$ which, for a completely random distribution of equal concentrations of Nb^{5+} and Ti^{4+} on these two sites, would electrostatically balance the excess positive charge of the W^{6+} cation. However, if Ti is in the Nb/Ti1 site, the Nb/Ti2 site would preferentially comprise Nb to maintain this balance. Therefore significant short-range order is predicted that would result in the refined atom positions in these chains representing average positions and hence give rise to high IDPs which are seen for the cations in ESI,† Table S2. Since we have assigned single parameters for both cations and anions to aid stability, we are unable to probe whether there exists a difference between ions at the edges and centre of the blocks. In general, the BVS values are acceptable for such a complex structure with variations around the Nb/Ti sites depending on possible local order introduced by the partial occupancy. Although it is noted that Nb2 (positioned centrally within the 4 × 4 blocks) appears significantly over-bonded (BVS = 6.5), the

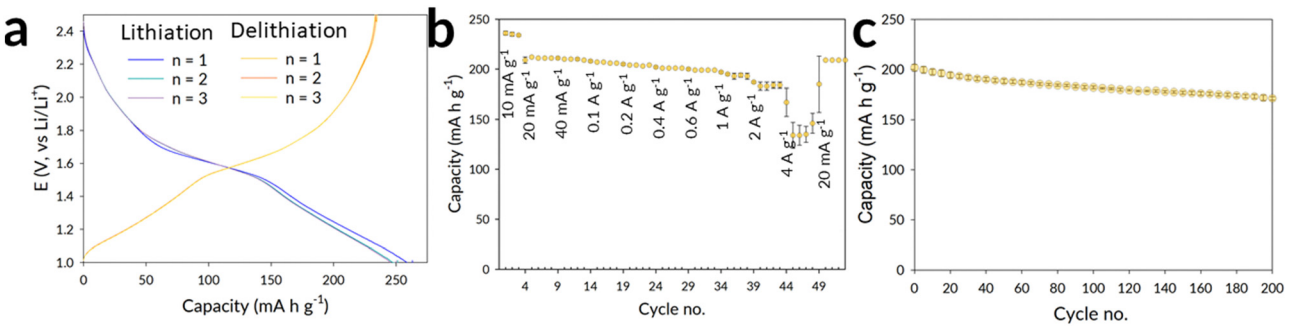

Fig. 3 (a) Galvanostatic discharge–charge curves of $Nb_9Ti_{1.5}W_{1.5}O_{30}$ in a Li half-cell format, with an applied current equivalent to 10 mA g^{-1} (cycle number denoted by *n*). (b) Resulting capacities of two cells undergoing rate testing. (c) Cycle life through symmetric cycling at 600 mA g^{-1}, over 200 cycles. Error bars are included in (b) and (c) and determined by taking the standard deviation of duplicate data.

low precision for most bond distances yield imprecise BVS values with esd values of ~0.4.

The material was then probed for its electrochemical performance within a Li half-cell, to evaluate its high rate capability. Initial formation cycles were conducted at 10 mA g^{-1} for all cells, before the commencement of lifetime and rate-testing. The formation curves of one cell is presented in Fig. 3a, and the dQ/dV shown in the ESI.† The first average lithiation and delithiation capacities were found to be 260 (3) and 236 (2) mA h g^{-1} the difference within these values is likely to be the result of lithium trapping with the large cavities (as shown in Fig. 2b). A reduced difference between the lithiation and delithiation capacity is noted in the second and third formation cycles, where the values converge in the rate-testing study applied to the same two cells (Fig. 3b). The asymmetric rate testing[25] involved applying a constant lithiation rate of 0.1 A g^{-1}, with the delithiation rate increasing every 5 cycles from: 0.02, 0.04, 0.1, 0.2, 0.4, 0.6, 1, 2, 4 A g^{-1}, before returning to 0.02 A g^{-1}. The dQ/dV relating to the rate-testing is shown in the ESI.†

At the higher current rates, with a current density of 2 A g^{-1} and 4 A g^{-1}, an average delithiation capacity (across the rate step of 5 cycles) of 184 (4) and 143 (17) mA h g^{-1} was achieved. In the perspective of time, the current densities of 2 A g^{-1} and 4 A g^{-1} correspond to a delithiation time of 5 and 2 minutes, respectively. The material's cycle life was also considered (Fig. 3c), with the fabrication of a further two cells. In this testing procedure, post formation, the (de)lithiation was set as 0.6 A g^{-1}. Over 100 cycles, the capacity retention is found to be 90%, with a further 5% reduction at the 200th cycle.

To conclude, a dual-doped (Ti, W) niobium oxide is structurally elucidated through combined neutron and X-ray diffraction refinements, defining a novel block structure with W fully occupying a site at the edge of the block, close to two sites with an even distribution of one Ti and one Nb. With respect to electrochemical performance, good capacities are achieved, with the most significant at the higher current rates, where a capacity of 184 (4) mA h g^{-1} is obtained at a high current of 2 A g^{-1}.

While not only highlighting a new material, the reduction in the usage of a critical material (*i.e.* W) compared to recently reported Nb–W–O systems, while delivering comparable performance, offers future opportunities in considering solid solution mixtures (preliminary additional compositional studies of $Nb_{12-x}Ti_xW_xO_{30}$ are presented in the ESI†).

Conceptualization: EHD, PRS. Data Curation: EHD, AJG, DF, CH. Formal Analysis: EHD, CG. Investigation: EHD. Methodology: EHD, LLD, DF, CH, EK, CG. Visualization: EHD, CG. Validation: EHD. Supervision: EK, CG, PRS. Writing – original draft: EHD, DF, CG, PRS. Writing – review & editing: EHD, EK, CG and PRS.

The authors would like to thank the ISIS facility for provision of beam time *via* the Xpress access route (RB2291041) and the HRPD instrument scientists (DF and CH) for carrying out the data collection and reduction. We would like to acknowledge the following bodies for funding this work: School of Chemistry PhD Scholarship (EHD) and The Faraday Institution project grants (FITG045 and FIIF-019).

Data availability

Data for this article, including: SEM images, and EDS count maps, electrochemical testing, XRPD, and neutron diffraction is available on The University of Birmingham Institutional Research Archive (UBIRA) at **https://edata.bham.ac.uk/1121**.

Conflicts of interest

There are no conflicts to declare.

Notes and references

1 C. Pillot, Avicenne Energy, presented in part at the Batteries Event 2021, France, September 2021.
2 T. F. Yi, L. J. Jiang, J. Shu, C. B. Yue, R. S. Zhu and H. Bin Qiao, *J. Phys. Chem. Solids*, 2010, **71**, 1236–1242.
3 H. Liu, Z. Zhu, Q. Yan, S. Yu, X. He, Y. Chen, R. Zhang, L. Ma, T. Liu, M. Li, R. Lin, Y. Chen, Y. Li, X. Xing, Y. Choi, L. Gao, H. S. Yun Cho, K. An, J. Feng, R. Kostecki, K. Amine, T. Wu, J. Lu, H. L. Xin, S. P. Ong and P. Liu, *Nature*, 2020, **585**, 63–67.
4 R. Roth, B. Gatehouse and A. Wadsley, *Naturwissenschaften*, 1964, **51**, 262–263.
5 R. Roth and A. Wadsley, *Acta Crystallogr.*, 1965, **19**, 26–32.
6 A. J. Green, E. H. Driscoll, Y. Lakhdar, E. Kendrick and P. R. Slater, *Dalton Trans.*, 2023, **52**, 13110–13118.
7 K. J. Griffith, Y. Harada, S. Egusa, R. M. Ribas, R. S. Monteiro, R. B. Von Dreele, A. K. Cheetham, R. J. Cava, C. P. Grey and J. B. Goodenough, *Chem. Mater.*, 2021, **33**, 4–18.
8 L. L. Driscoll, E. H. Driscoll, B. Dong, F. N. Sayed, J. N. Wilson, C. A. O'Keefe, D. J. Gardner, C. P. Grey, P. K. Allan, A. A. L. Michalchuk and P. R. Slater, *Energy Environ. Sci.*, 2023, **16**, 5196–5209.
9 K. J. Griffith, A. C. Forse, J. M. Griffin and C. P. Grey, *J. Am. Chem. Soc.*, 2016, **138**, 8888–8899.
10 J. T. Han, Y. H. Huang and J. B. Goodenough, *Chem. Mater.*, 2011, **23**, 2027–2029.
11 X. Wu, J. Miao, W. Han, Y. S. Hu, D. Chen, J. S. Lee, J. Kim and L. Chen, *Electrochem. Commun.*, 2012, **25**, 39–42.
12 C. Yang, S. Deng, C. Lin, S. Lin, Y. Chen, J. Li and H. Wu, *Nanoscale*, 2016, **8**, 18792–18799.
13 K. J. Griffith, K. M. Wiaderek, G. Cibin, L. E. Marbella and C. P. Grey, *Nature*, 2018, **559**, 556–563.
14 X. H. Ma, X. Cao, Y. Y. Ye, F. Qiao, M. F. Qian, Y. Y. Wei, Y. D. Wu, Z. F. Zi and J. M. Dai, *Solid State Ionics*, 2020, **353**, 115376.
15 M. Wörle and F. Krumeich, *Z. Anorg. Allg. Chem.*, 2021, **647**, 98–106.
16 J. M. Sieffert, C. J. Lang, S. Bazylevych, S. Jia and E. McCalla, *J. Mater. Chem. A*, 2023, **12**, 1429–1437.
17 M. Grohol, C. V. Z. Grow and European Commission, Study on the Critical Raw Materials for the EU 2023.
18 S. Andersson, *J. Inorg. Gen. Chem.*, 1967, **351**, 106–112.
19 F. E. Rohrer and A. K. Larsson, *Acta Crystallogr., Sect. B: Struct. Sci.*, 2000, **56**, 780–784.
20 R. Norrin and B. Nolander, *Acta Chem. Scand.*, 1971, **25**, 741–743.
21 J. Perl, J. Shin, J. Schü Mann, B. Faddegon and H. Paganetti, *Med. Phys.*, 2012, **39**, 6818–6837.
22 B. Faddegon, J. Ramos-Méndez, J. Schue Mann, A. McNamara, J. Shin, J. Perl and H. Paganetti, *Phys. Medica*, 2020, **72**, 114–121.
23 B. H. Toby and R. B. Von Dreele, *J. Appl. Crystallogr.*, 2013, **46**, 544–549.
24 M. Kunz and I. David Brown, *J. Solid State Chem.*, 1995, **115**, 395–406.
25 Y. Lakhdar, H. Geary, M. Houck, D. Gastol, A. S. Groombridge, P. R. Slater and E. Kendrick, *ACS Appl. Energy Mater.*, 2022, **5**, 11229–11240.

